npj | climate and atmospheric science

www.nature.com/npjclimatsci

ARTICLE OPEN

Check for updates

Global increase in wildfire potential from compound fire weather and drought

Doug Richardson[1]✉, Amanda S. Black[1,2], Damien Irving[1], Richard J. Matear[1], Didier P. Monselesan[1], James S. Risbey[1], Dougal T. Squire[1] and Carly R. Tozer[1]

Wildfire can cause significant adverse impacts to society and the environment. Weather and climate play an important role in modulating wildfire activity. We explore the joint occurrence of global fire weather and meteorological drought using a compound events framework. We show that, for much of the globe, burned area increases when periods of heightened fire weather compound with dry antecedent conditions. Regions associated with wildfire disasters, such as southern Australia and the western USA, are prone to experiencing years of compound drought and fire weather. Such compound events have increased in frequency for much of the globe, driven primarily by increases in fire weather rather than changes in precipitation. El Niño Southern Oscillation is associated with widespread, spatially compounding drought and fire weather. In the Northern Hemisphere, a La Niña signature is evident, whereas El Niño is associated with such events in the tropics and, to a lesser degree, the Southern Hemisphere. Other climate modes and regional patterns of atmospheric circulation are also important, depending on the region. We show that the lengths of the fire weather seasons in eastern Australia and western North America have increased substantially since 2000, raising the likelihood of overlapping fire weather events in these regions. These cross-hemispheric events may be linked to the occurrence of El Niño, although the sea-surface temperature magnitudes are small. Instead, it is likely that anthropogenic climate change is the primary driver of these changes.

npj Climate and Atmospheric Science (2022)5:23 ; https://doi.org/10.1038/s41612-022-00248-4

INTRODUCTION

Wildfire can have severe environmental and societal impacts, affecting ecosystems, agricultural lands and urban settlements[1–4]. Recent high-profile disasters, such as those in Chile and Portugal in 2017[5,6], Greece in 2018[7], California in 2018 and 2020[8,9], and Australia in 2019–20[10] highlight the ongoing need for wildfire adaptation and mitigation strategies[11].

Variations in weather and climate influence wildfire activity by modulating vegetation production and fuel aridity[12]. Precipitation deficits induce moisture stress, increasing the flammability of fuel[13–15]. Yet the relationship between drought and wildfire varies markedly, with distinct differences dependent on the ecosystem[15,16]. In grasslands and savannas, drought is associated with decreased wildfire potential[3,17,18]. Antecedent precipitation promotes vegetation growth, yielding an abundance of available fuel that becomes flammable in the dry season. In these ecosystems, then, drought during the wet season results in a fuel-limited environment, suppressing the ability of wildfire to spread[15]. It is these frequent, low-intensity wildfires that account for the majority of burned area globally[19].

Conversely, in forest biomes, drought is associated with increased wildfire activity through a reduction in fuel moisture content[3,14,17,18,20–23]. Pertinently, the majority of economically or socially disastrous wildfires occur in temperate and boreal forest[3]. This suggests that drought plays a role in the costliest wildfire events. Multi-year drought was a major contributing factor to the severity of the 2019–20 wildfire season in Australia[24–27]. Wet-season precipitation deficits, combined with above-average fuel loads, have been implicated in the 2018 California wildfires[8].

Fire weather, which is characterised by high temperatures, low humidity and strong winds, is an important driver of wildfire across much of the globe[3,28–34]. As a product of multiple processes, fire weather is a form of compound event. Wind plays a crucial role in determining wildfire behaviour, affecting fire spread, intensity and ignition likelihood[15]. Wind, temperature and relative humidity can exacerbate flammability by warming and drying fuels[15]. Together with recent precipitation, these variables are often combined as fire weather indices, which are used routinely in wildfire management[35,36]. In many wildfire disaster-prone regions, such as western North America, the Mediterranean and southeast Australia, fire weather has become more frequent and more severe[34,37–45].

Moreover, anthropogenic climate change has extended the length of the fire weather season for many regions[39,46–49]. Future projections indicate this trend will continue[40,42,50–53]. This poses challenges for managing firefighting resources across regions that historically have distinctly separate wildfire seasons. The USA, Canada, Australia and New Zealand cooperate through shared firefighting resources such as equipment and personnel[10,54,55]. In the 2019–20 Australian fire season, hundreds of overseas firefighters were deployed to assist operations, and 11 of the 12 large air tankers used were sourced internationally[10]. In response, the Australian Royal Commission into National Natural Disaster Arrangements[10] specifically highlighted that lengthening fire seasons in the northern and southern hemispheres may reduce the availability of aircraft services to Australia. The severity of the following USA wildfire season further underlines these concerns. In 2020 major wildfires continued well through boreal autumn and into winter[56,57]. The season ended with over four million hectares burned, including more than 4% of California[9,58,59]. Fortunately, the 2019–20 wildfires in Australia and the subsequent 2020 USA wildfires were separated by a number of months. Concurrent

[1]CSIRO Oceans & Atmosphere, Castray Esplanade, Hobart, TAS 7004, Australia. [2]International Laboratory for High-Resolution Earth System Prediction, Texas A&M University, College Station, TX, USA. ✉email: doug.richardson@csiro.au

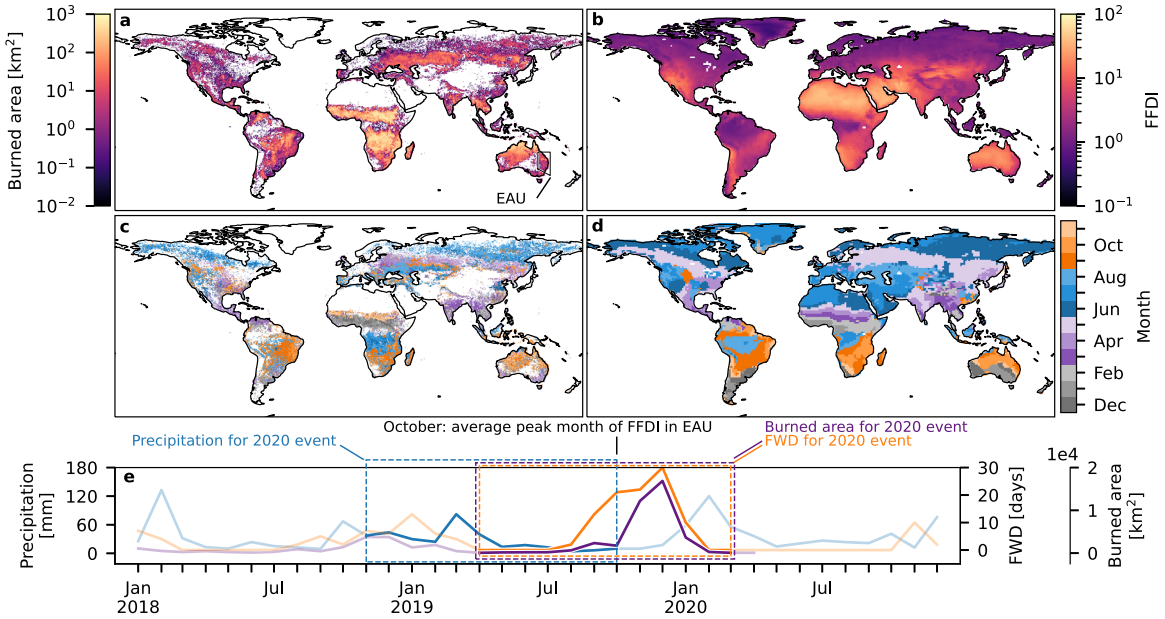

Fig. 1 FFDI and burned area climatology 2001–2019, and event definitions. a Average annual burned area (km^2). **b** Average daily FFDI. **c** Month of maximum average burned area. **d** Month of maximum average FFDI. **e** Example of which months are used in the calculation of annual values of precipitation, burned area and fire weather days (FWD). The data are for the eastern Australia (EAU) region shown in (**a**). October is the month of average maximum FFDI. Therefore the 2020 event is defined using the period November 2018 through October 2019 for precipitation, and April 2019 through March 2020 for FWD and burned area.

wildfires of similar severity to those events could place significant pressure on international cooperation.

The interaction of drought and fire weather constitutes a "compound event". The field of compound events has gained significant research interest in recent years, with the recognition that a combination of multiple hazards or drivers can amplify impacts[60–67].

There are numerous studies on "hot and dry" compound extremes, the majority of which focus on precipitation deficits and high temperatures over a common period, for example hot and dry summers[43,68–77]. Consideration of hazards over different time scales is less common, although some studies assess the joint behaviour of daily temperature extremes and seasonal precipitation[66,78,79]. Furthermore, the studies that explicitly consider fire weather and drought only consider the latter on time-scales of at most 3 months[43,66,74]. This neglects the long-term processes that can be associated with increased wildfire potential in some regions. An exception to this is a study that assessed the role of annual precipitation and monthly fire weather during the Australian 2019–20 fire season[34].

Although the role of drought and extreme fire weather in driving wildfire potential is well known, the preceding discussion highlights that these hazards are often considered independently. Furthermore, many such analyses are regional, and do not consider the possibilities of synchronous wildfire potential in multiple regions. The extent to which extreme fire weather and drought compound, and how their co-occurrence has changed through time, has not been explored on a global scale.

In this article, we explore the relationship between global fire weather and long-term antecedent meteorological drought. Using the Forest Fire Danger Index (FFDI, see "Methods") and accumulated precipitation, we quantify the co-occurrence of these two hazards, identify regional "hot spots" and trends, and analyse potential climate drivers. We follow the definitions provided in a recent typology of compound events to differentiate between sub-classes of compound events[67]. A hazard that causes or amplifies an impact only as a consequence of a preceding hazard is known as a "preconditioned event". Here, meteorological drought is considered the precondition that might amplify the impact caused by a period of heightened fire weather.

We also discuss the simultaneous occurrence of these hazards across different regions. Hazards that occur in different regions within a time frame so as to cause an impact are classed as "spatially compounding events"[67]. We address the growing concerns of lengthening fire weather seasons in the USA and Australia by analysing changes in spatially compounding fire weather and drought in these nations. We will also explore possible drivers of these events by considering a range of climate modes associated with fire weather in these regions.

RESULTS

Relationship of burned area to fire weather and antecedent precipitation

The FFDI is highest on average in desert regions that do not feature wildfires (Fig. 1a, b). This is not surprising given that temperature and relative humidity are components of the index. There is a clear correspondence between the seasonality of burned area and FFDI (Fig. 1c, d). The months that, on average, yield the maximum burned area and FFDI are often the same. Otherwise, in places such as southern Australia and western North America, the maximum FFDI leads the maximum burned area by a month or more, suggesting that wildfires are most widespread following the peak of the fire weather season.

We define a "fire weather day" (FWD) as when the FFDI exceeds the climatological 95th percentile. This threshold is calculated using all data (i.e., not as a function of month or season), so the vast majority of fire weather days occur during the fire season[45]. The number of fire weather days accumulated over some period, L, is denoted FWD_L. We similarly estimate drought using accumulated precipitation, P_L.

We consider annual statistics to analyse preconditioned drought and fire weather events. Using the peak FFDI months shown in Fig. 1d, we target the 12-month period best suited to estimating the severity of the fire weather season and the magnitude of a preceding drought. For annual fire weather, FWD_L,

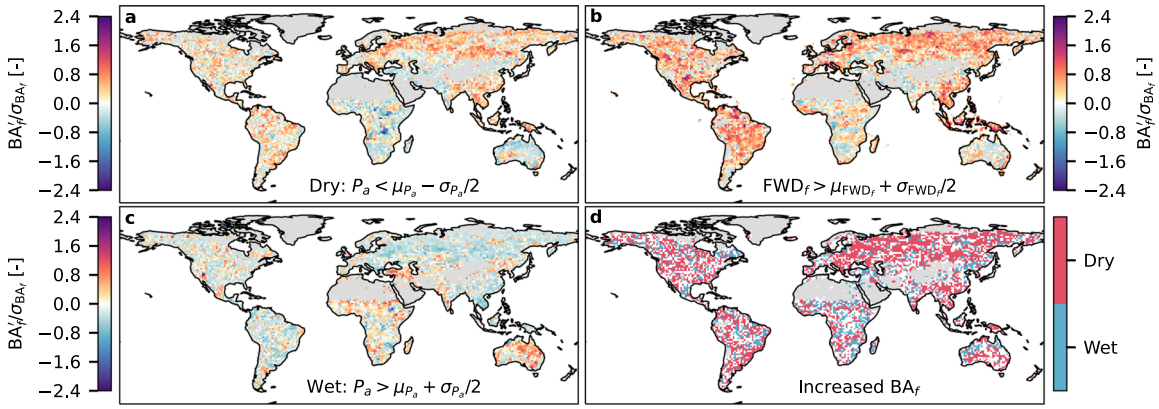

Fig. 2 Relationship of burned area to fire weather and precipitation. a Annual normalised burned area anomalies, $(BA_f)'/\sigma_{BA_f}$ (dashes indicate anomalies), for 2001–2019, averaged over dry antecedent years, defined as when $P_a < \mu_{P_a} - \sigma_{P_a}/2$. For most grid cells, five to seven years satisfy this threshold. **b** As in **a** but for years of heightened fire weather, defined as when $FWD_f > \mu_{FWD_f} + \sigma_{FWD_f}/2$. **c** As in **a** but for wet antecedent years, $P_a > \mu_{P_a} + \sigma_{P_a}/2$. **d** Grid cells for which burned area anomalies increase when wet (blue; **c**) or dry (red; **a**) years compound with years of heightened fire weather (**b**). White indicates no increase in burned area from compound dry or wet years. There are typically only one to three of these compound years, but results are robust when computed with smaller departures from the mean e.g. using $\mu \pm \sigma/4$.

we set $L = f$, where f denotes the "fire year". This is the 12-month period from six months prior to five months following the peak FFDI month. We also utilise satellite-derived burned area data, which we accumulate over the same period and denote as BA_f. For annual precipitation, P_L, we choose an antecedent period, $L = a$. This period encompasses the 12 months leading up to and including the peak FFDI month, providing an estimate of fuel dryness at the peak of the fire weather season. Therefore, the extent to which a "year" can be classified as a preconditioned event includes data from an 17-month period, and is labelled according to the year of the last month in that period.

An illustration of these quantities is shown in Fig. 1e, for the eastern Australia (EAU) region of the Intergovernmental Panel on Climate Change (IPCC) regions[80]. For denoting spatially-averaged quantities, we use a superscript indicating the region, r. The month of average maximum $FFDI^{EAU}$ is October. Therefore, antecedent precipitation, P_a^{EAU}, is accumulated for November through October. Fire weather days, FWD_f^{EAU}, are accumulated for April through March. The example in Fig. 1e, for the 2020 event, highlights the lack of precipitation leading up to the fire season, particularly during the preceding winter. Also shown is the high precipitation in February 2020 that was critical in extinguishing many of the wildfires, with the burned area reducing to virtually zero. The number of fire weather days was high throughout the warm season. This peaked in December, with all but one day classed as a fire weather day (also found for a region southward of EAU by another study[45]).

We find that annual variations in fire weather exert greater influence on burned area than variations in antecedent precipitation. Years with anomalously high numbers of fire weather days correspond to greater burned area anomalies than years of anomalous antecedent precipitation (Fig. 2a–c). There is a positive relationship between burned area and fire weather for much of the globe, including North and South America, Europe and large swathes of Asia (Fig. 2b). The relationship between accumulated precipitation and burned area is more varied. Dry conditions appear to be a factor in increased burned area for tropical forested regions such as the Amazon and the Maritime Continent (Fig. 2a), in agreement with other studies[21,81,82]. Increased precipitation prior to the peak fire weather season is associated with positive burned area anomalies in much of Australia and parts of Africa and the Mediterranean (Fig. 2c), due to the promotion of fine fuel growth[3,17,18]. Regarding Australia, note that in the southeast coastal strip, where the majority of national wildfire disasters occur, burned area anomalies are positive for dry antecedent conditions and for higher numbers of fire weather days. The short burned area record (20 years) means these results should be treated cautiously. In particular, a permutation test shows that the results described here for dry and wet years are not statistically significant for many grid cells (Supplementary Figure 1).

For most of the globe, burned area during years with anomalously high fire weather is increased when the preceding year has been drier than average (Fig. 2d). In a few regions, such as northwest Australia and Madagascar, heightened fire weather preceded by a wetter-than-average year is associated with increased burned area. This highlights the importance of considering compound climate extremes in relation to wildfire potential. As wildfire potential in most regions is exacerbated by heightened fire weather compounding with antecedent dry conditions, our focus for the remainder of the paper is on compound drought and fire weather.

Compound drought and fire weather events

We define a "drought year" as when accumulated precipitation is less than one standard deviation below the mean, $P_a < \mu_{P_a} - \sigma_{P_a}$. Similarly, a "fire weather year" is defined as when $FWD_f > \mu_{FWD_f} + \sigma_{FWD_f}$. There are clear "hot spots" in which preconditioned drought and fire weather years occur (Fig. 3a). This includes regions that suffer from wildfire disasters, such as western North America, the Mediterranean and southeast Australia. Furthermore, in these regions the number of preconditioned events has increased since 1996 (Fig. 3b).

Using six IPCC regions as an illustration, we find that increases in the frequency of preconditioned events appear to be driven primarily by changes in fire weather rather than drought (Fig. 3c–h). In western North America (WNA), there have been eight fire weather years since 1990, but only two of these coincide with drought. Similarly, a steep rise in fire weather days in western South Africa (WSAF) since 2000 is mitigated by increased precipitation, hence only two preconditioned event years. The Mediterranean (MED), on the other hand, has seen six preconditioned event years since 2000, driven by declining precipitation and an apparent step change in the frequency of fire weather days. A possible step change is also evident in southern Australia (SAU). Siberia has experienced significant wildfires in recent years[83], and we find record high numbers of fire weather days in eastern Siberia (ESB) in 2017 and 2018. Increased wildfire potential from an upward trend in fire weather days is, however, moderated by increased precipitation.

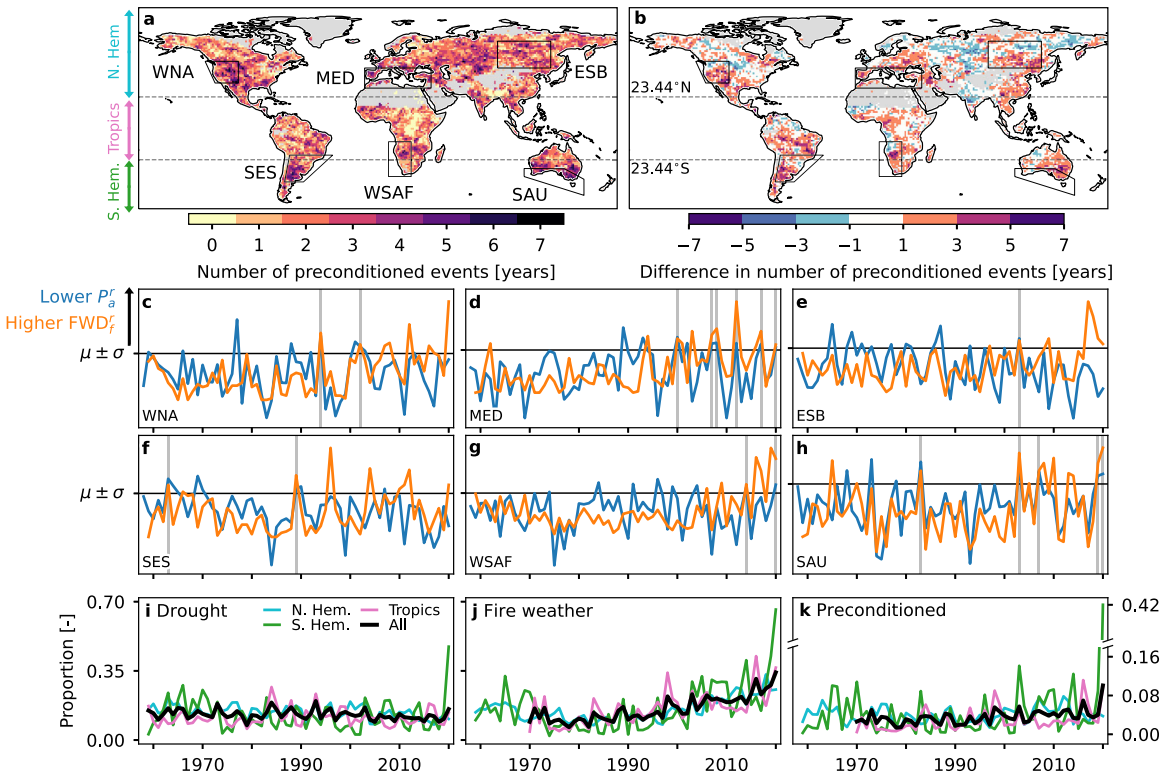

Fig. 3 Climatology and changes in preconditioned drought and fire weather. a Number of preconditioned drought $P_a < \mu_{P_a} - \sigma_{P_a}$ and fire weather $FWD_f > \mu_{FWD_f} + \sigma_{FWD_f}$ years 1970–2020. **b** Change in number of preconditioned drought and fire weather years from 1971-1995 to 1996-2020. **c–h** Annual number of fire weather days, FWD_f^r (orange), and antecedent precipitation, P_a^r (blue), for six IPCC regions. The data are scaled to have unit variance and adjusted such that the threshold for drought ($\mu_{P_a^r} - \sigma_{P_a^r}$) and fire weather ($\mu_{FWD_f^r} + \sigma_{FWD_f^r}$) years are the same. The *y*-axis for precipitation is inverted such that both drought and fire weather years lie above the threshold (the black horizontal line labelled $\mu \pm \sigma$). Preconditioned drought and fire weather years are indicated by vertical grey lines. **i-k** Proportion of area in drought, fire weather, and preconditioned years, respectively. Colours indicate data for the Northern Hemisphere, the Southern Hemisphere, the tropics, and global.

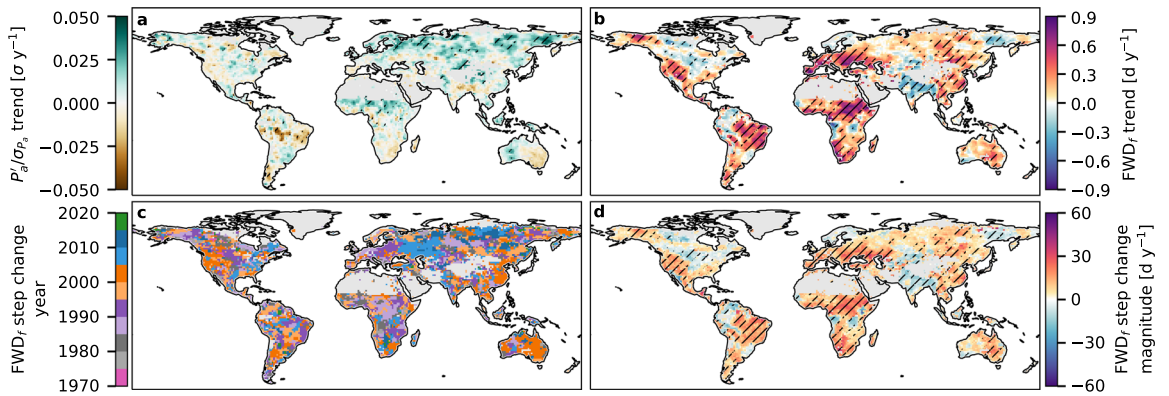

Fig. 4 Fire weather and precipitation trends and change points 1970–2020. a Theil-Sen slope for normalised annual antecedent precipitation anomalies, P'/σ_{P_a} (dashes indicate anomalies). **b** As in **a** but for annual numbers of fire weather days, FWD_f. Hatching in (**a**) and (**b**) indicates a statistically significant result for the Mann-Kendall test for monotonic trends. **c** Pettitt test year of potential step change in annual numbers of fire weather days FWD_f. **d** Pettitt test step change magnitude for FWD_f. Hatching in (**d**) indicates statistical significance for the Pettitt test.

To further investigate the nature of these changes, we apply statistical tests for monotonic trends and change points in precipitation and fire weather ("Methods"). Although annual precipitation has changed for some regions, we do not find sufficient statistical support for trends (Fig. 4a) or step changes (Supplementary Fig. 3) in most regions. The exception to this is in parts of high-latitude Europe and Asia, which show significant increases in precipitation of up to 0.5 standard deviations per year. For fire weather days, we find evidence of increasing trends and change points for many parts of the world, including western North America, Brazil, eastern Europe and western Asia, and southeast Australia (Fig. 4b–d). Furthermore, step changes in several key regions (western North America, the Mediterranean and southeast Australia) occurred at around the same time, in the 1990s to early 2000s (Fig. 4c), in agreement with findings from regional studies[37,45].

For regions that now experience more frequent occurrences of fire weather days, the change appears to be driven by higher daily

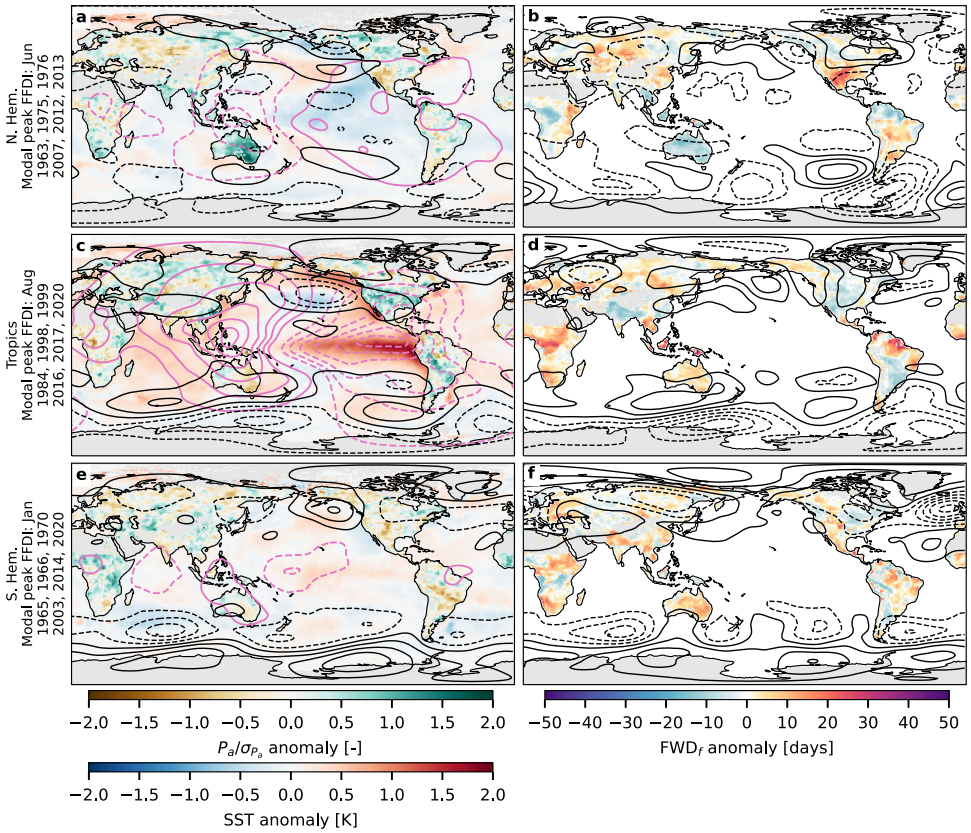

Fig. 5 Composites of spatially extensive preconditioned drought and fire weather years. a Normalised antecedent precipitation (P_a/σ_{P_a}; brown and green shading), sea surface temperature (SST; red and blue shading), 500 hPa geopotential heights (z_{500}; black contours starting at ± 5 m and spaced in intervals of 10 m) and 200 hPa velocity potential (ϕ_{200}; pink contours starting at ± 5e5 m^2s^{-1} and spaced in intervals of 5e5 m^2s^{-1}). The data are anomalies averaged over the six years listed to the left of the panel, selected as the 10% of years with the most widespread drought and fire weather in the Northern Hemisphere. **b** As in (**a**) but for fire weather day, FWD_f, anomalies (shading) and three-monthly z_{500} anomalies (contours starting at ± 5 m and spaced in intervals of 10 m). **c–f** As in (**a**) and (**b**) but for the tropics and the Southern Hemisphere. In all panels, precipitation and fire weather data are for the "fire year" ($L = f$) and "antecedent" ($L = a$) periods, respectively, which vary spatially (see the text and Fig. 1d). The period used for other variables in the left (right) column is the 12 (three) months ending (centred) on the most common peak FFDI month for the Northern Hemisphere (June), tropics (August), or Southern Hemisphere (January). Solid (dashed) contours indicate positive (negative) anomalies.

maximum temperatures and lower daily relative humidity (Supplementary Fig. 4). Decreases in fire weather days, for example in India and northeastern Russia, appear to be driven primarily by increased relative humidity, which overrides increases in maximum daily temperature.

The dominant role of the FFDI in driving widespread increases in preconditioned drought and fire weather events is also evident globally at the grid-cell scale. The proportion of area in drought in any given year has remained steady since 1959, perhaps undergoing a slight decrease (Fig. 3i). The number of fire weather days, on the other hand, has increased since 1980 (Fig. 3j). These differing trends combine to result in an increase in preconditioned events (Fig. 3k). In 2019–20, drought afflicted almost 50% of the Southern Hemisphere, with almost 70% affected by extreme fire weather conditions. A remarkable 42% suffered both drought and fire weather years in 2019–20, driven by how widespread the severe conditions were in Australia.

Drivers of preconditioned and spatially compounding events

We composite a number of atmospheric and oceanic diagnostics on the 10% of years (six years) that featured the most widespread preconditioned drought and fire weather conditions (Fig. 3i–k). Due to the contrasting fire weather seasons, we consider the Northern Hemisphere, the tropics and the Southern Hemisphere separately.

In the Northern Hemisphere, the six most widespread preconditioned years feature precipitation deficits and more numerous fire weather days across western-central Russia and Kazakhstan, eastern Asia and southern and eastern North America (Fig. 5a, b). Pacific SST anomalies during the 12 months prior to the peak of the fire weather season resemble La Niña and negative Pacific Decadal Oscillation (PDO) signatures (Fig. 5a), consistent with the regional relationships between these modes and precipitation[84–89]. Large-scale anomalies of velocity potential at 200 hPa (ϕ_{200}; Fig. 5a) indicate associated changes in the Walker circulation, which in turn is linked to reduced precipitation in southern North America and increased precipitation over Australia. During May, June and July of these years, positive 500 hPa geopotential height (z_{500}) anomalies suggest atmospheric ridging or blocking played a role in the heightened fire weather in northwestern Asia and North America (Fig. 5b). This is consistent with other studies: ridging is a feature of North America fire spread events[90] and increased wildfire potential[91–94], while a long-lived block was implicated in the 2010 western Russia heatwave and wildfires[95,96].

The signal from the z_{500} anomaly composite, however, suffers from substantial smoothing of local features. Due to the large land area of the Northern Hemisphere (compared to the tropics or the Southern Hemisphere), there is greater variability amongst the members of the composite shown in Fig. 5a, b. The locations of simultaneous fire weather "hot spots" across the hemisphere vary

between individual years. The common feature of these events regardless of where they occur is that nodes of positive z_{500} anomalies are co-located with areas of heightened fire weather (Supplementary Fig. 5). Furthermore, on individual years, analysis of 300 hPa zonal and meridional wind provides evidence of circumglobal wave trains with a wavenumber ranging between five and seven. This suggests that spatially compounding fire weather events may be linked to recurrent Rossby wave patterns. Indeed, it has been shown that Rossby waves with wavenumbers five and seven are linked to simultaneous summer heatwaves across the hemisphere[97–99].

Preconditioned drought and fire weather years in the tropics have become more widespread over time, with five of the six years with the highest proportion of affected area occurring since 1998 (Figs. 3k and 5c, d). In agreement with other studies[21,69,89,100–103], a strong El Niño signature is associated with drought affecting western and central Africa, the Maritime Continent and northeastern South America (Fig. 5c and Supplementary Fig. 6). Positive ϕ_{200} anomalies over the western Pacific and eastern Indian Ocean indicate upper-level convergence, associated with a weakening of the ascending branch of the Walker circulation. This can result in a weakened boreal summer monsoon and is associated with drought across the tropics[103]. Indeed drought, more so than fire weather, is regarded as a key climate driver of wildfire potential in tropical rainforest[81,82,104–107].

Southern Hemisphere preconditioned events span southern South Africa and southeast Australia, with a mixed response in southern South America (Fig. 5e, f). A much weaker El Niño pattern is evident compared to tropical preconditioned events (Fig. 5e). Analysis of the individual years in the composite reveals a combination of El Niño- and La Niña-like SST patterns (Supplementary Fig. 7). This is perhaps due to the differing responses to ENSO across the Southern Hemisphere. While El Niño tends to be related to drought and extreme fire weather in southeast Australia[32,34,108,109], ENSO impacts on precipitation and temperature in southern African and southern South America are multifaceted, dependent on the stage of the ENSO cycle and on the season[102,110–112].

Since the tropical regions are not providing a unique pattern to force concurrent extratropical extremes, we look to the large-scale atmospheric circulation to see if it might assume this role. Positive z_{500} anomalies are evident over Antarctica, with negative anomalies to the north, in the 12-month period leading to the peak fire season (February through January) and the 3-month period centred over this peak (December through February). This feature resembles the negative phase of the Southern Annular Mode[113] (SAM), which can be associated with reduced precipitation in southern Australia and southeastern South Africa[34,114,115]. In southern South America, however, enhanced wildfire activity can be associated with the opposite (positive) phase of the SAM[116,117]. This is consistent with our findings, which show a reduction in the number of fire weather days in this region (Fig. 5f). Coincident with the negative-phase SAM, we also find evidence of a wave train with wavenumber four that may link coincident fire weather anomalies across the hemisphere (Fig. 5f). Wave trains with wavenumbers four or five are evident in the individual years (Supplementary Fig. 7). This supports previous research which established that these wavenumbers are associated with amplified wave resonance and circumglobal, spatially compounding temperature extremes in austral summer[97].

Spatially compounding fire weather in western North America and eastern Australia

In this section we focus on changes in overlapping fire weather seasons in western North America (WNA) and eastern Australia (EAU). We switch to monthly data, calculating three-month accumulations of fire weather days and burned area (denoted FWD_3^r and BA_3^r, respectively), and 12-month accumulations of precipitation (P_{12}^r). These accumulations are calculated on a rolling basis and are right-labelled according to the last month of the accumulation period. Similarly to the previous section, we consider a fire weather or burned area (drought) event as a month which exceeds (is below) one standard deviation from the mean.

The mid-1970s to the late 1990s was a relatively quiescent period for fire weather in both regions. From 2000 the number of fire weather events dramatically increases (Fig. 6), consistent with trend and step change results for these regions found here (Fig. 4) and in other studies[31,33,39,42,45,118,119].

As a consequence, the two regions are now far more likely to experience prolonged periods of increased fire weather in the same year (Fig. 6). Between 1958 and 2000, there were three years during which WNA and EAU both experienced at least three fire weather events (indicated by the pink squares below the top panel of Fig. 6). Such years occurred eight times in the remaining 20 years from 2001, including three consecutive years between 2017 and 2019. Moreover, there has been an increase in the number of overlapping (concurrent) fire weather events across

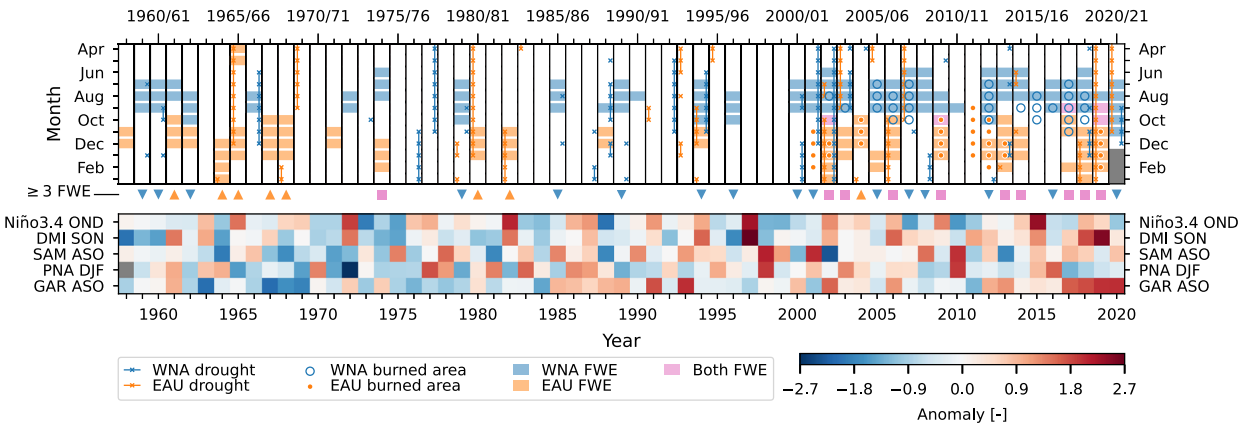

Fig. 6 Fire weather, drought and burned area in western North America (WNA) and eastern Australia (EAU), and related climate modes. Top Fire weather events, $FWD_3^r > \mu_{FWD_3^r} + \sigma_{FWD_3^r}$ (rectangles); burned area events, $BA_3^r > \mu_{BA_3^r} + \sigma_{BA_3^r}$ (open and filled circles); and drought events, $P_{12}^r < \mu_{P_{12}^r} - \sigma_{P_{12}^r}$ (vertical lines with cross markers). Years in which there were at least three fire weather events (FWE) in a region are marked with a triangle or square below. WNA results are in blue, EAU results are in orange, and concurrent results are in pink. Bottom The Niño3.4 index, the dipole mode index (DMI), the southern annular mode index (SAM), the Pacific-North America pattern index (PNA) and the Gulf of Alaska ridge index (GAR), averaged over the three months indicated by the last three letters.

regions, with one occurrence prior to 2000, and seven after 2000 (pink rectangles in the top panel). These overlaps typically occur in October, but the Septembers of 2017 and 2019 are also concurrent events. The prolonged USA fire weather season of 2020 is evident, with five consecutive fire weather events, including the first such November on record. These results complement a previous study, which showed that between 1973 and 2013 the length of fire weather seasons in California increased, and the frequency of long fire weather seasons in eastern Australia and western North America has increased over the same period[48].

Spatially compounding fire weather in these two regions is associated with El Niño-like SSTs in October through December. This is evidenced by the positive Niño3.4 values for eight of the 11 years featuring at least three fire weather events in both regions (pink squares; Fig. 6). In eastern Australia, years of increased wildfire potential are typically associated with El Niño[32,34,108,120]. Accordingly, we find that six of nine years with at least three fire weather events in EAU (orange triangles) feature an El Niño-like pattern. On the other hand, of the 14 such years in WNA, nine feature La Niña-like SSTs (blue triangles). The mixed response of WNA fire weather to ENSO accords with other regional studies, which show substantial differences across the western USA[121–125].

In addition to El Niño, we find that years of increased fire weather days in EAU tend to be associated with a positive phase IOD and negative phase SAM (Fig. 6). The role of these three modes in promoting Australian wildfire potential is well established[32,34,108,120]. In particular, it is the co-occurrence of fire-promoting phases of these modes that may be crucial, rather than their magnitudes[34]. Our findings accord with this—while the majority of years with at least three EAU fire weather events feature these modes in their fire-promoting phase, their averaged magnitudes are not large (no greater than |0.8|) and are not statistically distinct from zero.

The Pacific North America (PNA) pattern[126] is associated with fluctuations in the East Asia jet stream. In its positive phase, the PNA is associated with increased temperatures and reduced precipitation in western North America[127–129]. Similar circulation characteristics have been identified during large fire years[93] and years of increased climate-related wildfire potential[92]. However, we find no evidence of this, with years featuring at least three WNA fire weather events just as likely to feature a negative winter PNA index as a positive index (Fig. 6). Due to the association of local ridges with fire events in the region[43,90], we use the Gulf of Alaska ridge (GAR) index[130,131] to indicate anomalous upper-level high-pressure activity. We find that boreal autumn (ASO) values of the GAR index are generally positive during years with at least three WNA fire weather events, suggesting enhanced anticyclonic circulation and meridional shifts in the jet stream.

DISCUSSION

We have analysed changes in wildfire potential related to compound fire weather and meteorological drought. Regions prone to wildfire disasters, including southern Australia, the Mediterranean, and the western USA, are among the most likely to experience fire weather years preconditioned by drought. Furthermore, much of the globe has experienced an increase in such events, driven by changes in fire weather rather than precipitation.

Our analysis shows that the likelihood of spatially compounding fire weather in western North America (WNA) and eastern Australia (EAU) has increased. In both regions, the number of fire weather events (three-month periods with anomalously high numbers of fire weather days) has increased substantially in the past two decades. As a result, these regions have become more likely to experience prolonged periods of heightened fire weather, with a greater likelihood of the fire weather seasons overlapping.

ENSO is a key driver of global drought and fire weather. Its warm phase, El Niño, is strongly associated with preconditioned events in the tropics, most likely due to its moderating effects on monsoonal precipitation[103]. An El Niño signature is comparatively weaker for Southern Hemisphere preconditioned events, emerging as a composite from both El Niño- and La Niña-like SST patterns, in line with the differing continental responses to ENSO. The key feature associated with drought and fire weather in the Southern Hemisphere is a negative SAM-like pattern. This pattern is evident throughout both austral summer and the preceding year, and is consistent with reduced precipitation and heightened fire weather in southern Australia and South Africa. In contrast, Northern Hemisphere preconditioned events are associated with La Niña. Atmospheric ridging and blocking is also evident at higher latitudes in boreal summer, supporting previous research highlighting the importance of jet stream variability in modulating wildfire activity[90].

Although La Niña tends to coincide with increased fire weather in the Northern Hemisphere, spatially compounding events in WNA and EAU are associated with El Niño. The average magnitudes of ENSO and other, more local, climate modes are small for these events. It is possible that the co-occurrence of fire-promoting phases of these modes is important, rather than their individual magnitudes[32,34]. Alternatively, the role of the modes discussed here may be relatively inconsequential in relation to spatially compounding fire weather events.

Our finding that upward trends in climate-related wildfire potential is driven by increasingly severe fire weather likely reflects the impacts of anthropogenic climate change. Higher temperatures are sufficient to increase wildfire potential, and future wildfire regimes are likely to be driven by temperature rather than rainfall[132,133]. Rising mean and extreme temperatures[134], and increasing atmospheric aridity[135], are linked to increases in fuel dryness, resulting in more frequent and severe wildfires[4,9,31,49,136]. Future projections of wildfire are region-dependent and subject to substantial uncertainties. But, in general, models point toward an increase in burned area for wildfire-prone regions such as western North America, southern Australia and the Mediterranean[3,4,132,137], emphasising the continuing requirement for adaptation to changing wildfire patterns[11].

METHODS

Fire weather, drought and burned area

The McArthur Forest Fire Danger Index[35,138] (FFDI) is calculated as

$$\mathrm{FFDI} = D^{0.987}\exp(0.0338T - 0.0345H + 0.0234W + 0.243147), \quad (1)$$

where T (°C) is the maximum daily 2m temperature, H (%) is the daily average 2m relative humidity, W (km/h) is the maximum daily 10m wind speed. The "drought factor", D, is the rolling 20-day total precipitation, scaled to range between zero and 10, with larger D for lower precipitation totals. We use the Japanese 55-year reanalysis product[139] (JRA55), which provides data from 1958 to 2020 at a spatial resolution of 1.25° latitude and longitude. Very similar formulations of the FFDI have been used in studies of fire weather in Australia[34,45]. We chose to use the FFDI over indices from other major fire danger rating systems as it is simpler to compute and interpret. The Canadian Fire Weather Index is more widely used than the FFDI, but has more stringent requirements for its calculation[36]. For example, the index considers the possible effect of snowmelt affecting wildfire potential. Given that our study is focused primarily on the meteorological aspects of fire weather, we opted to use the FFDI.

We find that FFDI data in tropical regions is unstable in the early part of the record. Extremely high FFDI values, driven by very high T and W, and very low H, are present at various times for a large proportion of tropical grid cells before 1970. These values are often by far the greatest in magnitude throughout the entire record. We therefore exclude data for tropical grid cells (between the Tropic of Cancer, 23.44°N, and the Tropic of Capricorn, 23.44°S) before 1970.

To quantify fire weather over a given period, L, we accumulate the number of days on which the FFDI is above the climatological 95th percentile, calculated using all available data. Such days are called "fire weather days" (FWDs). On an annual basis, we accumulate fire weather days over a 12-month period that begins six months prior to, and ends five months after, the peak fire weather month. The peak fire weather month is determined as the month that yields the average maximum FFDI, as shown in Fig. 1d. Annual accumulations of fire weather days are denoted FWD_f, where $L = f$ indicates the "fire year". Regionally-averaged quantities are denoted with a superscript indicating the region, r, i.e. FWD_f^r. For monthly analyses, fire weather days are accumulated on a right-labelled rolling three-month basis, denoted FWD_3^r.

We use satellite-derived monthly burned area data from FireCCI v5.1, provided by the European Space Agency Climate Change Initiative[140] and C3S v1.0 from the Copernicus Climate Change Service. These data are provided on a 0.25° grid between 2001 and April 2020. Burned area is accumulated over different periods in the same way as for fire weather days: BA_f and BA_3^r are defined using the same periods as their fire weather day equivalent.

We quantify drought using monthly precipitation from the Global Precipitation Climatology Centre (GPCC) dataset[141] for 1957–2020. These data are derived from quality-controlled station gauge data, and are provided over land with a resolution of 0.25° latitude and longitude. As with fire weather days and burned area, we consider annual and monthly statistics. We estimate annual drought severity at the height of the fire season by accumulating precipitation in the 12 months leading up to the peak FFDI month. This quantity is denoted P_a, where the period $L = a$ indicates the antecedent conditions. For monthly analyses of regional averages, right-labelled rolling 12-month accumulations are used, denoted P_{12}^r.

Throughout the manuscript we apply a mask to remove grid cells with zero total burned area (Fig. 1a). Data sets with coarser resolution than the burned area data are first aggregated to the required resolution by summing all burned area grid cells within each coarser grid cell.

Compound event definitions

We use FWD_f, FWD_f^r, P_a and P_a^r to analyse annual changes in fire weather and drought. A "fire weather year" is defined as when $\mathrm{FWD}_f > \mu_{\mathrm{FWD}_f} + \sigma_{\mathrm{FWD}_f}$. Similarly a "drought year" is when $P_a < \mu_{P_a} - \sigma_{P_a}$. We deem a preconditioned drought and fire weather year to occur when both these conditions are satisfied. Superscripts are used in the usual way for the regional equivalents.

For the monthly analysis of fire weather in eastern Australia (EAU) and western North America (WNA), we define events in a similar way. A "fire weather (burned area) event" is a month in which FWD_3^r (BA_3^r) exceeds one standard deviation above the mean, i.e. $\mathrm{FWD}_3^r > \mu_{\mathrm{FWD}_3^r} + \sigma_{\mathrm{FWD}_3^r}$ or $\mathrm{BA}_3^r > \mu_{\mathrm{BA}_3^r} + \sigma_{\mathrm{BA}_3^r}$. A "drought event" is a month in which P_{12}^r is less that one standard deviation below the mean, $P_{12}^r < \mu_{P_{12}^r} - \sigma_{P_{12}^r}$.

Trend and change point testing

The Mann-Kendall trend test[142,143] is a rank correlation test between the ranks of the observations and their temporal ordering. For a time series $\mathbf{X} = \{X_1, X_2, \ldots, X_T\}$, the test statistic, S, is given by:

$$S = \sum_{i=1}^{T-1} \sum_{j=i+1}^{T} \mathrm{sgn}(X_j - X_i), \tag{2}$$

where

$$\mathrm{sgn}(X_j - X_i) = \begin{cases} 1, & x_i < x_j \\ 0, & x_i = x_j \\ -1, & x_i > x_j. \end{cases} \tag{3}$$

The Pettitt test[144] is a non-parametric used to identify possible step changes in a time series. The series $\mathbf{X}$ is said to have a change point at τ if X_t for $t = 1, \ldots, \tau$ have a common distribution function $F_1(x)$ and X_t for $t = \tau + 1, \ldots, T$ have a common distribution function $F_2(x)$, and $F_1(x) \neq F_2(x)$. The null hypothesis of "no change", H_0: $\tau = T$, is tested against the alternative hypothesis of "change", H_1: $1 \leq \tau < T$, using the statistic

$$K_T = \max_{1 \leq t < T} |U_{t,T}|, \tag{4}$$

where

$$U_{t,T} = \sum_{i=1}^{t} \sum_{j=i+1}^{T} \mathrm{sgn}(X_i - X_j). \tag{5}$$

The Mann-Kendall and Pettitt tests assume the data are independent and identically distributed. This assumption is often not satisfied for meteorological data, which can exhibit serial dependence. We apply a block bootstrap procedure[145–148] to try and mitigate the effects of autocorrelation. The block bootstrap randomly resamples "blocks" of length B. We assume that the data follow a first-order autoregressive process[147]. Then B is calculated as

$$B = (n - B + 1)^{(2/3)(1 - n'/n)}, \tag{6}$$

where n' is the effective sample size given by

$$n' \approx n \frac{1 - \rho_1}{1 + \rho_1}, \tag{7}$$

and ρ_1 is the lag-1 autocorrelation coefficient. This procedure is applied to each grid cell, so B varies spatially. In our case B ranges between 1 and 11 for both P_a and FWD_f (Supplementary Fig. 2).

We generate 1000 block-bootstrapped series of the same length as the original series and calculate the quantile q at which the test statistic (S or K_T) calculated from the original data lies in the bootstrapped sample. The p value is then $p = 1 - q$.

To account for spatial autocorrelation and multiple testing, we control the false discovery rate[149] (FDR). The FDR approach ranks the p values from the N tests in ascending order, $p_{(1)}, \ldots p_{(N)}$. A test is considered statistically significant if $p < p_{\mathrm{FDR}}$, where

$$p_{\mathrm{FDR}} = \max_{j = 1, \ldots, N} \left\{ p_{(j)} : p_{(j)} \leq \frac{j}{N} \alpha_{\mathrm{FDR}} \right\}. \tag{8}$$

We choose $\alpha_{\mathrm{FDR}} = 0.1$, allowing, on average, for 10% of statistically significant results to be erroneous (i.e. the null hypotheses are true).

Alongside Mann-Kendall statistical significance results, in Fig. 4 we show the magnitude of the trend estimated using the Theil-Sen estimator[150]. The Theil-Sen estimator is the median of all slopes between paired values. For the Pettitt test, we present the year of a change point (regardless of statistical significance) and the magnitude, computed as the difference in median FWD_f between the period after, and prior to, the change point year.

Climate diagnostics

We obtain monthly sea-surface temperature (SST) data for 1958–2020 from the UK Met Office Hadley Centre Sea Ice and Sea Surface Temperature data set[151]. Atmospheric diagnostics are from JRA55. We use 500 hPa geopotential heights (z_{500}) as an indicator of the mid-tropospheric circulation, zonal and meridional wind at 300 hPa (u_{300} and v_{300}) as diagnostics of the upper-level circulation, and velocity potential at 200 hPa (ϕ_{200}) as a measure of upper-level divergence and convergence. All data are aggregated to monthly means. We obtain anomalies by removing the monthly mean calculated over 1958–2020.

In Fig. 5, fire weather day and precipitation anomalies are accumulated over the periods f and a, respectively, as described earlier. As such, this period varies spatially. For SST and the atmospheric variables, however, we use a common period for all grid cells to avoid averaging over a number of different periods. We choose the period based on the most common peak FFDI month for the Northern Hemisphere (June), the tropics (August) and the Southern Hemisphere (January). Twelve-month anomalies (left column) are averaged from six months before, to five months after, the listed months. Three-month anomalies (right column) are centred on the listed months.

We calculate indices for five climate modes. To represent El Niño Southern Oscillation (ENSO), we use the Niño3.4 index[152], which is the average SST anomaly over 5°N-5°S, 120°-170°W. The Indian Ocean Dipole (IOD) is represented using the Dipole Mode Index[153] (DMI). The DMI is the difference between SST anomalies averaged over western (10°N-10°S, 50°-70°E) and south-eastern (0°-10°S, 90°-110°E) regions in the Indian Ocean. The Southern Annular Mode (SAM) is represented using an index defined as the difference between the normalised mean sea-level pressure at 40°S and 60°S[113]. The Pacific-North America pattern (PNA) index[126] is calculated as $\mathrm{PNA} = (z_1 - z_2 + z_3 - z_4)/4$, where z_1, z_2, z_3 and z_4 are the z_{500} anomalies at 20°N, 160°W; 45°N, 165°W; 55°N, 115°W; and 30°N, 85°W; respectively. The Gulf of Alaska ridge (GAR) index[130,131] is calculated as 200 hPa

geopotential height anomalies averaged over the domain 45°-55°N, 145°-135°W.

In Fig. 6, these indices are presented as three-month averages. The months were chosen as those that yield the greatest correlation with December FWD_3^{EAU} (for Niño3.4, DMI and SAM) or August FWD_3^{WNA} (for GAR). As the PNA is typically considered a winter phenomenon[126–129], and winter values of the index have been related to wildfire by other studies[92,93], December through February was chosen as the appropriate period for this index.

DATA AVAILABILITY

Reanalysis data are from the Japanese Meteorological Agency 55-year reanalysis product[139], publicly available at https://rda.ucar.edu/datasets/ds628.0/. The European Space Agency FireCCI v5.1[140] and Copernicus Climate Change Service C3S v1.0 burned area data is available at https://cds.climate.copernicus.eu/cdsapp#!/dataset/satellite-fire-burned-area. Precipitation data are from the Global Precipitation Climatology Centre[141], available at https://www.dwd.de/EN/ourservices/gpcc/gpcc.html. Sea surface temperature data are from the UK Met Office Hadley Centre[151] at https://www.metoffice.gov.uk/hadobs/hadisst/.

CODE AVAILABILITY

The codes used for this work are openly available at https://doi.org/10.5281/zenodo.5911970.

Received: 14 July 2021; Accepted: 21 February 2022;
Published online: 25 March 2022

REFERENCES

1. Gill, A. M., Stephens, S. L. & Cary, G. J. The worldwide "wildfire" problem. *Ecol. Appl.* **23**, 438–454 (2013). Publisher: John Wiley & Sons, Ltd.
2. Moritz, M. A. et al. Learning to coexist with wildfire. *Nature* **515**, 58–66 (2014).
3. Bowman, D. M. J. S. et al. Human exposure and sensitivity to globally extreme wildfire events. *Nat. Ecol. Evolut.* **1**, 1–6 (2017). Number: 3 Publisher: Nature Publishing Group.
4. Bowman, D. M. J. S. et al. Vegetation fires in the Anthropocene. *Nat. Rev. Earth Environ.* (2020). https://doi.org/10.1038/s43017-020-0085-3.
5. de la Barrera, F., Barraza, F., Favier, P., Ruiz, V. & Quense, J. Megafires in Chile 2017: Monitoring multiscale environmental impacts of burned ecosystems. *Sci. Total Environ.* **637-638**, 1526–1536 (2018).
6. Turco, M. et al. Climate drivers of the 2017 devastating fires in Portugal. *Sci. Rep.* **9**, 13886 (2019). Number: 1 Publisher: Nature Publishing Group.
7. Lagouvardos, K., Kotroni, V., Giannaros, T. M. & Dafis, S. Meteorological Conditions Conducive to the Rapid Spread of the Deadly Wildfire in Eastern Attica, Greece. *Bull. Am. Meteorological Soc.* **100**, 2137–2145 (2019). Publisher: American Meteorological Society Section: Bulletin of the American Meteorological Society.
8. Brown, T., Leach, S., Wachter, B. & Gardunio, B. The Extreme 2018 Northern California Fire Season. *Bull. Am. Meteorological Soc.* **101**, S1–S4 (2020). Publisher: American Meteorological Society Section: Bulletin of the American Meteorological Society.
9. Higuera, P. E. & Abatzoglou, J. T. Record-setting climate enabled the extraordinary 2020 fire season in the western United States. *Glob. Change Biol.* **27**, 1–2 (2021).
10. Royal Commission into National Natural Disaster Arrangements. Royal Commission into National Natural Disaster Arrangements - Report. Tech. Rep. (2020). https://naturaldisaster.royalcommission.gov.au/publications/royal-commission-national-natural-disaster-arrangements-report.
11. Cochrane, M. A. & Bowman, D. M. J. S. Manage fire regimes, not fires. *Nat. Geosci.* **14**, 455–457 (2021).
12. Bradstock, R. A. A biogeographic model of fire regimes in Australia: current and future implications. *Glob. Ecol. Biogeogr.* **19**, 145–158 (2010).
13. Cochrane, M. A. Fire science for rainforests. *Nature* **421**, 913–919 (2003). Number: 6926 Publisher: Nature Publishing Group.
14. Abatzoglou, J. T., Williams, A. P., Boschetti, L., Zubkova, M. & Kolden, C. A. Global patterns of interannual climate-fire relationships. *Glob. Change Biol.* **24**, 5164–5175 (2018).
15. Pausas, J. G. & Keeley, J. E. Wildfires and global change. Frontiers in Ecology and the Environment n/a (2021). https://doi.org/10.1002/fee.2359.
16. Littell, J. S., McKenzie, D., Peterson, D. L. & Westerling, A. L. Climate and wildfire area burned in western U.S. ecoprovinces, 1916-2003. *Ecol. Appl.* **19**, 1003–1021 (2009).
17. Westerling, A. L., Gershunov, A., Brown, T. J., Cayan, D. R. & Dettinger, M. D. Climate and Wildfire in the Western United States. *Bull. Am. Meteorological Soc.* **84**, 595–604 (2003). Publisher: American Meteorological Society Section: Bulletin of the American Meteorological Society.
18. Barbero, R., Abatzoglou, J. T., Steel, E. A. & Larkin, N. K. Modeling very large-fire occurrences over the continental United States from weather and climate forcing. *Environ. Res. Lett.* **9**, 124009 (2014). Publisher: IOP Publishing.
19. van der Werf, G. R. et al. Interannual variability in global biomass burning emissions from 1997 to 2004. *Atmos. Chem. Phys.* **6**, 3423–3441 (2006). Publisher: Copernicus GmbH.
20. Gedalof, Z., Peterson, D. L. & Mantua, N. J. Atmospheric, climatic, and ecological controls on extreme wildfire years in the Northwestern United States. *Ecol. Appl.* **15**, 154–174 (2005).
21. Chen, Y. et al. A pan-tropical cascade of fire driven by El Niño/Southern Oscillation. *Nat. Clim. Change* **7**, 906–911 (2017). Number: 12 Publisher: Nature Publishing Group.
22. Ruffault, J., Curt, T., Martin-StPaul, N. K., Moron, V. & Trigo, R. M. Extreme wildfire events are linked to global-change-type droughts in the northern Mediterranean. *Nat. Hazards Earth Syst. Sci.* **18**, 847–856 (2018). Publisher: Copernicus GmbH.
23. Madadgar, S., Sadegh, M., Chiang, F., Ragno, E. & AghaKouchak, A. Quantifying increased fire risk in California in response to different levels of warming and drying. *Stoch. Environ. Res. Risk Assess.* **34**, 2023–2031 (2020).
24. Nolan, R. H. et al. Causes and consequences of eastern Australia's 2019-20 season of mega-fires. *Glob. Change Biol.* **26**, 1039–1041 (2020).
25. Adams, M. A., Shadmanroodposhti, M. & Neumann, M. Causes and consequences of Eastern Australia's 2019-20 season of mega-fires: A broader perspective. *Glob. Change Biol.* **26**, 3756–3758 (2020).
26. Bradstock, R. A. et al. A broader perspective on the causes and consequences of eastern Australia's 2019-20 season of mega-fires: A response to Adams et al. *Glob. Change Biol.* **26**, e8–e9 (2020).
27. King, A. D., Pitman, A. J., Henley, B. J., Ukkola, A. M. & Brown, J. R. The role of climate variability in Australian drought. *Nat. Clim. Change* **10**, 177–179 (2020). Number: 3 Publisher: Nature Publishing Group.
28. Hoffmann, W. A., Schroeder, W. & Jackson, R. B. Regional feedbacks among fire, climate, and tropical deforestation. Journal of Geophysical Research: Atmospheres 108 (2003). https://doi.org/10.1029/2003JD003494.
29. Bedia, J. et al. Global patterns in the sensitivity of burned area to fire-weather: Implications for climate change. *Agric. For. Meteorol.* **214-215**, 369–379 (2015).
30. Fang, L., Yang, J., Zu, J., Li, G. & Zhang, J. Quantifying influences and relative importance of fire weather, topography, and vegetation on fire size and fire severity in a Chinese boreal forest landscape. *For. Ecol. Manag.* **356**, 2–12 (2015).
31. Williams, A. P. et al. Observed Impacts of Anthropogenic Climate Change on Wildfire in California. *Earth's Future* **7**, 892–910 (2019).
32. Abram, N. J. et al. Connections of climate change and variability to large and extreme forest fires in southeast Australia. *Commun. Earth Environ.* **2**, 1–17 (2021). Number: 1 Publisher: Nature Publishing Group.
33. Canadell, J. G. et al. Multi-decadal increase of forest burned area in Australia is linked to climate change. *Nat. Commun.* **12**, 6921 (2021).
34. Squire, D. T. et al. Likelihood of unprecedented drought and fire weather during Australia's 2019 megafires. *npj Clim. Atmos. Sci.* **4**, 1–12 (2021).
35. Luke, R. H. & McArthur, A. G. *Bush Fires in Australia.* (Australian Government Publishing Service, Canberra, ACT, 1978).
36. van Wagner, C. Development and structure of the Canadian Forest Fire Weather Index System. Tech. Rep. 35, Candian Forestry Service (1987). https://cfs.nrcan.gc.ca/publications?id=19927.
37. Moreno, M. V., Conedera, M., Chuvieco, E. & Pezzatti, G. B. Fire regime changes and major driving forces in Spain from 1968 to 2010. *Environ. Sci. Policy* **37**, 11–22 (2014).
38. Dupire, S., Curt, T. & Bigot, S. Spatio-temporal trends in fire weather in the French Alps. *Sci. Total Environ.* **595**, 801–817 (2017).
39. Jain, P., Wang, X. & Flannigan, M. D. Trend analysis of fire season length and extreme fire weather in North America between 1979 and 2015. *Int. J. Wildland Fire* **26**, 1009–1020 (2018). Publisher: CSIRO PUBLISHING.
40. Abatzoglou, J. T., Williams, A. P. & Barbero, R. Global emergence of anthropogenic climate change in fire weather indices. *Geophys. Res. Lett.* **46**, 326–336 (2019).
41. Urbieta, I. R., Franquesa, M., Viedma, O. & Moreno, J. M. Fire activity and burned forest lands decreased during the last three decades in Spain. *Ann. For. Sci.* **76**, 90 (2019).

42. Goss, M. et al. Climate change is increasing the likelihood of extreme autumn wildfire conditions across California. *Environ. Res. Lett.* **15**, 094016 (2020). Publisher: IOP Publishing.
43. Abatzoglou, J. T., Rupp, D. E., O'Neill, L. W. & Sadegh, M. Compound extremes drive the western oregon wildfires of september 2020. *Geophys. Res. Lett.* **48**, e2021GL092520 (2021).
44. Giannaros, T. M., Kotroni, V. & Lagouvardos, K. Climatology and trend analysis (1987-2016) of fire weather in the Euro-Mediterranean. *Int. J. Climatol.* **41**, E491–E508 (2021).
45. Richardson, D. et al. Increased extreme fire weather occurrence in southeast Australia and related atmospheric drivers. *Weather Clim. Extremes* **34**, 100397 (2021).
46. Wotton, B. M. & Flannigan, M. D. Length of the fire season in a changing climate. *Forestry Chron.* **69**, 187–192 (1993). Publisher: Canadian Institute of Forestry.
47. Clarke, H., Lucas, C. & Smith, P. Changes in Australian fire weather between 1973 and 2010. *Int. J. Climatol.* **33**, 931–944 (2013).
48. Jolly, W. M. et al. Climate-induced variations in global wildfire danger from 1979 to 2013. *Nat. Commun.* **6**, 7537 (2015).
49. Abatzoglou, J. T. & Williams, A. P. Impact of anthropogenic climate change on wildfire across western US forests. *Proc. Natl Acad. Sci.* **113**, 11770–11775 (2016). Publisher: National Academy of Sciences Section: Physical Sciences.
50. Williams, A. A. J., Karoly, D. J. & Tapper, N. The Sensitivity of Australian Fire Danger to Climate Change. *Climatic Change* **49**, 171–191 (2001).
51. Lucas, C., Hennessy, K., Mills, G. A. & Bathols, J. M. Bushfire weather in Southeast Australia recent trends and projected climate change impacts; consultancy report prepared for the Climate Institute of Australia. Tech. Rep., Bushfire Cooperative Research Centre, Australian Bureau of Meteorology and CSIRO Marine and Atmospheric Research, Melbourne, VIC (2007). https://doi.org/10.25919/5e31c82ee0a4c.
52. Clarke, H. G. et al. Regional signatures of future fire weather over eastern Australia from global climate models. *Int. J. Wildland Fire* **20**, 550–562 (2011). Publisher: CSIRO PUBLISHING.
53. Wotton, B. M., Flannigan, M. D. & Marshall, G. A. Potential climate change impacts on fire intensity and key wildfire suppression thresholds in Canada. *Environ. Res. Lett.* **12**, 095003 (2017). Publisher: IOP Publishing.
54. Global Fire Monitoring Center (GFMC). International Arrangements on the Sharing of Wildland Fire Suppression Resources between the United States of America and Australia and New Zealand. Tech. Rep., Global Fire Monitoring Center (GFMC), Freiburg, Germany (2003). https://gfmc.online/iffn/iffn_29/USA-Australia-NZ-Int-Arrangements.pdf.
55. European Policy Evaluation Consortium (EPEC). Study on wild fire fighting resources sharing models. Tech. Rep., European Policy Evaluation Consortium (EPEC), Brussels, Belgium (2010). https://ec.europa.eu/echo/files/civil_protection/civil/prote/pdfdocs/future/Wildfire_Final_Report.pdf.
56. Patel, K. East Troublesome Fire Spreads to the Rockies (2020). https://earthobservatory.nasa.gov/images/147452/east-troublesome-fire-spreads-to-the-rockies. Publisher: NASA Earth Observatory, https://earthobservatory.nasa.gov/images/147452/east-troublesome-fire-spreads-to-the-rockies.
57. Hansen, K. New Fires Scorch the Hills of Southern California (2020). https://earthobservatory.nasa.gov/images/147625/new-fires-scorch-the-hills-of-southern-california. Publisher: NASA Earth Observatory, https://earthobservatory.nasa.gov/images/147625/new-fires-scorch-the-hills-of-southern-california.
58. California Department of Forestry and Fire Protection. 2020 Fire Season (2021). https://www.fire.ca.gov/incidents/2020/.
59. National Interagency Fire Center. Wildfires and Acres (2021). https://www.nifc.gov/fire-information/statistics/wildfires.
60. Seneviratne, S. I. et al. Changes in Climate Extremes and their Impacts on the Natural Physical Environment. In *Managing the Risks of Extreme Events and Disasters to Advance Climate Change Adaptation*, A Special Report of Working Groups I and II of the Intergovernmental Panel on Climate Change (IPCC), 109-230 (Cambridge University Press, Cambridge University Press, Cambridge, UK and New York, NY, USA, 2012). https://www.ipcc.ch/site/assets/uploads/2018/03/SREX-Chap3_FINAL-1.pdf.
61. Leonard, M. et al. A compound event framework for understanding extreme impacts. *WIREs Clim. Change* **5**, 113–128 (2014). Publisher: John Wiley & Sons, Ltd.
62. Wahl, T., Jain, S., Bender, J., Meyers, S. D. & Luther, M. E. Increasing risk of compound flooding from storm surge and rainfall for major US cities. *Nat. Clim. Change* **5**, 1093–1097 (2015). Number: 12 Publisher: Nature Publishing Group.
63. Zscheischler, J. et al. Future climate risk from compound events. *Nat. Clim. Change* **8**, 469–477 (2018).
64. Hillier, J. K., Matthews, T., Wilby, R. L. & Murphy, C. Multi-hazard dependencies can increase or decrease risk. *Nat. Clim. Change* **10**, 595–598 (2020). Number: 7 Publisher: Nature Publishing Group.
65. Raymond, C. et al. Understanding and managing connected extreme events. *Nat. Clim. Change* **10**, 611–621 (2020). Number: 7 Publisher: Nature Publishing Group.
66. Ridder, N. N. et al. Global hotspots for the occurrence of compound events. *Nat. Commun.* **11**, 5956 (2020). Number: 1 Publisher: Nature Publishing Group.
67. Zscheischler, J. et al. A typology of compound weather and climate events. *Nat. Rev. Earth Environ.* **1**, 333–347 (2020). Number: 7 Publisher: Nature Publishing Group.
68. Zscheischler, J. & Seneviratne, S. I. Dependence of drivers affects risks associated with compound events. *Sci. Adv.* **3**, e1700263 (2017). Publisher: American Association for the Advancement of Science Section: Research Article.
69. Hao, Z., Hao, F., Singh, V. P. & Zhang, X. Quantifying the relationship between compound dry and hot events and El Niño-southern Oscillation (ENSO) at the global scale. *J. Hydrol.* **567**, 332–338 (2018).
70. Alizadeh, M. R. et al. A century of observations reveals increasing likelihood of continental-scale compound dry-hot extremes. *Sci. Adv.* **6**, eaaz4571 (2020).
71. Feng, S. et al. A database for characteristics and variations of global compound dry and hot events. *Weather Clim. Extremes* **30**, 100299 (2020).
72. Ribeiro, A. F. S., Russo, A., Gouveia, C. M., Páscoa, P. & Zscheischler, J. Risk of crop failure due to compound dry and hot extremes estimated with nested copulas. *Biogeosciences* **17**, 4815–4830 (2020). Publisher: Copernicus GmbH.
73. Ruffault, J. et al. Increased likelihood of heat-induced large wildfires in the Mediterranean Basin. *Sci. Rep.* **10**, 13790 (2020). Number: 1 Publisher: Nature Publishing Group.
74. Sutanto, S. J., Vitolo, C., Di Napoli, C., D'Andrea, M. & Van Lanen, H. A. Heatwaves, droughts, and fires: Exploring compound and cascading dry hazards at the pan-European scale. *Environ. Int.* **134**, 105276 (2020).
75. Zscheischler, J. & Fischer, E. M. The record-breaking compound hot and dry 2018 growing season in Germany. *Weather Clim. Extremes* **29**, 100270 (2020).
76. Markonis, Y. et al. The rise of compound warm-season droughts in Europe. *Sci. Adv.* **7**, eabb9668 (2021). Publisher: American Association for the Advancement of Science Section: Research Article.
77. Ionita, M., Caldarescu, D. E. & Nagavciuc, V. Compound Hot and Dry Events in Europe: Variability and Large-Scale Drivers. Frontiers in Climate 3 (2021). https://doi.org/10.3389/fclim.2021.688991/full. Publisher: Frontiers.
78. Ribeiro, A. F. S., Russo, A., Gouveia, C. M. & Pires, C. A. L. Drought-related hot summers: A joint probability analysis in the Iberian Peninsula. *Weather Clim. Extremes* **30**, 100279 (2020).
79. Vogel, J., Paton, E., Aich, V. & Bronstert, A. Increasing compound warm spells and droughts in the Mediterranean Basin. *Weather Clim. Extremes* **32**, 100312 (2021).
80. Iturbide, M. et al. An update of IPCC climate reference regions for sub-continental analysis of climate model data: definition and aggregated datasets. *Earth Syst. Sci. Data* **12**, 2959–2970 (2020). Publisher: Copernicus GmbH.
81. Nepstad, D. et al. Amazon drought and its implications for forest flammability and tree growth: a basin-wide analysis. *Glob. Change Biol.* **10**, 704–717 (2004).
82. van der Werf, G. R. et al. Climate regulation of fire emissions and deforestation in equatorial Asia. *Proc. Natl Acad. Sci.* **105**, 20350–20355 (2008). Publisher: National Academy of Sciences Section: Physical Sciences.
83. Ponomarev, E., Yakimov, N., Ponomareva, T., Yakubailik, O. & Conard, S. G. Current Trend of Carbon Emissions from Wildfires in Siberia. Atmosphere 12 (2021).
84. Mantua, N. J., Hare, S. R., Zhang, Y., Wallace, J. M. & Francis, R. C. A Pacific Interdecadal Climate Oscillation with Impacts on Salmon Production. *Bull. Am. Meteorological Soc.* **78**, 1069–1080 (1997). Publisher: American Meteorological Society Section: Bulletin of the American Meteorological Society.
85. Dai, A. & Wigley, T. M. L. Global patterns of ENSO-induced precipitation. *Geophys. Res. Lett.* **27**, 1283–1286 (2000).
86. Seager, R. et al. Mechanisms of ENSO-forcing of hemispherically symmetric precipitation variability. *Q. J. R. Meteorological Soc.* **131**, 1501–1527 (2005).
87. Mo, K. C. Interdecadal Modulation of the Impact of ENSO on Precipitation and Temperature over the United States. *J. Clim.* **23**, 3639–3656 (2010). Publisher: American Meteorological Society Section: Journal of Climate.
88. Newman, M. et al. The Pacific Decadal Oscillation, Revisited. *J. Clim.* **29**, 4399–4427 (2016). Publisher: American Meteorological Society Section: Journal of Climate.
89. Schubert, S. D. et al. Global Meteorological Drought: A Synthesis of Current Understanding with a Focus on SST Drivers of Precipitation Deficits. *J. Clim.* **29**, 3989–4019 (2016). Publisher: American Meteorological Society Section: Journal of Climate.
90. Jain, P. & Flannigan, M. The relationship between the polar jet stream and extreme wildfire events in North America. *J. Clim.* **-1**, 1–59 (2021). Publisher: American Meteorological Society Section: Journal of Climate.
91. Crimmins, M. A. Synoptic climatology of extreme fire-weather conditions across the southwest United States. *Int. J. Climatol.* **26**, 1001–1016 (2006).
92. Trouet, V., Taylor, A. H., Carleton, A. M. & Skinner, C. N. Fire-climate interactions in forests of the American Pacific coast. *Geophys. Res. Lett.* 33 (2006). https://doi.org/10.1029/2006GL027502.

93. Trouet, V., Taylor, A. H., Carleton, A. M. & Skinner, C. N. Interannual variations in fire weather, fire extent, and synoptic-scale circulation patterns in northern California and Oregon. *Theor. Appl. Climatol.* **95**, 349–360 (2009).
94. Petoukhov, V. et al. Alberta wildfire 2016: Apt contribution from anomalous planetary wave dynamics. *Sci. Rep.* **8**, 12375 (2018).
95. Matsueda, M. Predictability of Euro-Russian blocking in summer of 2010. Geophysical Research Letters 38 (2011). https://doi.org/10.1029/2010GL046557.
96. Schaller, N. et al. Influence of blocking on Northern European and Western Russian heatwaves in large climate model ensembles. *Environ. Res. Lett.* **13**, 054015 (2018). Publisher: IOP Publishing.
97. Kornhuber, K. et al. Summertime planetary wave resonance in the Northern and Southern Hemispheres. *J. Clim.* **30**, 6133–6150 (2017).
98. Kornhuber, K. et al. Extreme weather events in early summer 2018 connected by a recurrent hemispheric wave-7 pattern. *Environ. Res. Lett.* **14**, 054002 (2019). Publisher: IOP Publishing.
99. Kornhuber, K. et al. Amplified Rossby waves enhance risk of concurrent heatwaves in major breadbasket regions. *Nat. Clim. Change* **10**, 48–53 (2020).
100. Ronchail, J. et al. Interannual rainfall variability in the Amazon basin and sea-surface temperatures in the equatorial Pacific and the tropical Atlantic Oceans. *Int. J. Climatol.* **22**, 1663–1686 (2002).
101. Gu, G., Adler, R. F., Huffman, G. J. & Curtis, S. Tropical rainfall variability on interannual-to-interdecadal and longer time scales derived from the GPCP monthly product. *J. Clim.* **20**, 4033–4046 (2007). Publisher: American Meteorological Society Section: Journal of Climate.
102. Cai, W. et al. Climate impacts of the El Niño-Southern Oscillation on South America. *Nat. Rev. Earth Environ.* **1**, 215–231 (2020). Number: 4 Publisher: Nature Publishing Group.
103. Singh, J., Ashfaq, M., Skinner, C. B., Anderson, W. B. & Singh, D. Amplified risk of spatially compounding droughts during co-occurrences of modes of natural ocean variability. *npj Clim. Atmos. Sci.* **4**, 1–14 (2021). Number: 1 Publisher: Nature Publishing Group.
104. Nepstad, D. C. et al. Large-scale impoverishment of Amazonian forests by logging and fire. *Nature* **398**, 505–508 (1999). Number: 6727 Publisher: Nature Publishing Group.
105. Siegert, F., Ruecker, G., Hinrichs, A. & Hoffmann, A. A. Increased damage from fires in logged forests during droughts caused by El Niño. *Nature* **414**, 437–440 (2001).
106. Andela, N. & van der Werf, G. R. Recent trends in African fires driven by cropland expansion and El Niño to La Niña transition. *Nat. Clim. Change* **4**, 791–795 (2014). Number: 9 Publisher: Nature Publishing Group.
107. Alencar, A. A., Brando, P. M., Asner, G. P. & Putz, F. E. Landscape fragmentation, severe drought, and the new Amazon forest fire regime. *Ecol. Appl.* **25**, 1493–1505 (2015).
108. Wang, G. & Cai, W. Two-year consecutive concurrences of positive Indian Ocean Dipole and Central Pacific El Niño preconditioned the 2019/2020 Australian "black summer" bushfires. *Geosci. Lett.* **7**, 19 (2020).
109. Freund, M. B., Marshall, A. G., Wheeler, M. C. & Brown, J. N. Central Pacific El Niño as a Precursor to Summer Drought-Breaking Rainfall Over Southeastern Australia. *Geophys. Res. Lett.* **48**, e2020GL091131 (2021).
110. Nicholson, S. E. & Kim, J. The relationship of the El Niño-southern Oscillation to African rainfall. *Int. J. Climatol.* **17**, 117–135 (1997).
111. Grimm, A. M., Barros, V. R. & Doyle, M. E. Climate Variability in Southern South America Associated with El Niño and La Niña Events. *J. Clim.* **13**, 35–58 (2000). Publisher: American Meteorological Society Section: Journal of Climate.
112. Mason, S. J. El Niño, climate change, and Southern African climate. *Environmetrics* **12**, 327–345 (2001).
113. Gong, D. & Wang, S. Definition of Antarctic Oscillation index. *Geophys. Res. Lett.* **26**, 459–462 (1999).
114. Gillett, N. P., Kell, T. D. & Jones, P. D. Regional climate impacts of the Southern Annular Mode. Geophysical Research Letters 33 (2006). https://doi.org/10.1029/2006GL027721.
115. Silvestri, G. & Vera, C. Nonstationary Impacts of the Southern Annular Mode on Southern Hemisphere Climate. *J. Clim.* **22**, 6142–6148 (2009). Publisher: American Meteorological Society Section: Journal of Climate.
116. Holz, A. & Veblen, T. T. Variability in the Southern Annular Mode determines wildfire activity in Patagonia. Geophysical Research Letters 38 (2011). https://doi.org/10.1029/2011GL047674.
117. Holz, A. et al. Southern Annular Mode drives multicentury wildfire activity in southern South America. *Proc. Natl Acad. Sci.* **114**, 9552–9557 (2017). Publisher: National Academy of Sciences Section: Physical Sciences.
118. Dowdy, A. J. Climatological variability of fire weather in Australia. *J. Appl. Meteorol. Climatol.* **57**, 221–234 (2018).
119. Abatzoglou, J. T., Juang, C. S., Williams, A. P., Kolden, C. A. & Westerling, A. L. Increasing synchronous fire danger in forests of the Western United States. *Geophys. Res. Lett.* **48**, e2020GL091377 (2021).
120. Harris, S. & Lucas, C. Understanding the variability of Australian fire weather between 1973 and 2017. *PLOS ONE* **14**, e0222328 (2019). Publisher: Public Library of Science.
121. Schonher, T. & Nicholson, S. E. The Relationship between California Rainfall and ENSO Events. *J. Clim.* **2**, 1258–1269 (1989). Publisher: American Meteorological Society Section: Journal of Climate.
122. Smith, S. R., Green, P. M., Leonardi, A. P. & O'Brien, J. J. Role of Multiple-Level Tropospheric Circulations in Forcing ENSO Winter Precipitation Anomalies. *Monthly Weather Rev.* **126**, 3102–3116 (1998). Publisher: American Meteorological Society Section: Monthly Weather Review.
123. Heyerdahl, E. K., Brubaker, L. B. & Agee, J. K. Annual and decadal climate forcing of historical fire regimes in the interior Pacific Northwest, USA. *Holocene* **12**, 597–604 (2002). Publisher: SAGE Publications Ltd.
124. Kitzberger, T., Brown, P. M., Heyerdahl, E. K., Swetnam, T. W. & Veblen, T. T. Contingent Pacific-Atlantic Ocean influence on multicentury wildfire synchrony over western North America. *Proc. Natl Acad. Sci.* **104**, 543–548 (2007). Publisher: National Academy of Sciences Section: Physical Sciences.
125. Cook, B. I. et al. Revisiting the leading drivers of pacific coastal drought variability in the contiguous United States. *J. Clim.* **31**, 25–43 (2018). Publisher: American Meteorological Society Section: Journal of Climate.
126. Wallace, J. M. & Gutzler, D. S. Teleconnections in the geopotential height field during the Northern Hemisphere Winter. *Monthly Weather Rev.* **109**, 784–812 (1981). Publisher: American Meteorological Society Section: Monthly Weather Review.
127. Carleton, A. M., Carpenter, D. A. & Weser, P. J. Mechanisms of interannual variability of the Southwest United States Summer rainfall maximum. *J. Clim.* **3**, 999–1015 (1990). Publisher: American Meteorological Society Section: Journal of Climate.
128. Leathers, D. J., Yarnal, B. & Palecki, M. A. The Pacific/North American Teleconnection Pattern and United States Climate. Part I: Regional Temperature and Precipitation Associations. *J. Clim.* **4**, 517–528 (1991). Publisher: American Meteorological Society Section: Journal of Climate.
129. Lin, Y.-H., Hipps, L. E., Wang, S.-Y. S. & Yoon, J.-H. Empirical and modeling analyses of the circulation influences on California precipitation deficits. *Atmos. Sci. Lett.* **18**, 19–28 (2017).
130. Wang, S.-Y., Hipps, L., Gillies, R. R. & Yoon, J.-H. Probable causes of the abnormal ridge accompanying the 2013-2014 California drought: ENSO precursor and anthropogenic warming footprint. *Geophys. Res. Lett.* **41**, 3220–3226 (2014).
131. Yoon, J.-H. et al. Increasing water cycle extremes in California and in relation to ENSO cycle under global warming. *Nat. Commun.* **6**, 8657 (2015). Number: 1 Publisher: Nature Publishing Group.
132. Pechony, O. & Shindell, D. T. Driving forces of global wildfires over the past millennium and the forthcoming century. *Proc. Natl Acad. Sci.* **107**, 19167–19170 (2010).
133. Sanderson, B. M. & Fisher, R. A. A fiery wake-up call for climate science. *Nat. Clim. Change* **10**, 175–177 (2020).
134. Sippel, S., Meinshausen, N., Fischer, E. M., Székely, E. & Knutti, R. Climate change now detectable from any single day of weather at global scale. *Nat. Clim. Change* **10**, 35–41 (2020).
135. Byrne, M. P. & O'Gorman, P. A. Trends in continental temperature and humidity directly linked to ocean warming. *Proc. Natl Acad. Sci.* **115**, 4863 (2018).
136. Boer, M. M., Resco de Dios, V. & Bradstock, R. A. Unprecedented burn area of Australian mega forest fires. *Nat. Clim. Change* **10**, 171–172 (2020). Number: 3 Publisher: Nature Publishing Group.
137. Sharples, J. J. et al. Natural hazards in Australia: extreme bushfire. *Climatic Change* **139**, 85–99 (2016).
138. Noble, I. R., Gill, A. M. & Bary, G. A. V. McArthur's fire-danger meters expressed as equations. *Aust. J. Ecol.* **5**, 201–203 (1980).
139. Japan Meteorological Agency. JRA-55: Japanese 55-year Reanalysis, Daily 3-Hourly and 6-Hourly Data (2013). https://doi.org/10.5065/D6HH6H41.
140. Lizundia-Loiola, J., Otón, G., Ramo, R. & Chuvieco, E. A spatio-temporal active-fire clustering approach for global burned area mapping at 250m from MODIS data. *Remote Sens. Environ.* **236**, 111493 (2020).
141. Becker, A. et al. A description of the global land-surface precipitation data products of the Global Precipitation Climatology Centre with sample applications including centennial (trend) analysis from 1901-present. *Earth Syst. Sci. Data* **5**, 71–99 (2013). Publisher: Copernicus GmbH.
142. Mann, H. B. Nonparametric tests against trend. *Econometrica* **13**, 245–259 (1945). Publisher: [Wiley, Econometric Society].
143. Kendall, M. Rank correlation methods. Rank correlation methods (Griffin, Oxford, England, 1955).
144. Pettitt, A. N. A non-parametric approach to the change-point problem. *J. R. Stat. Soc. Ser. C. (Appl. Stat.)* **28**, 126–135 (1979). Publisher: [Wiley, Royal Statistical Society].
145. Kunsch, H. R. The Jackknife and the Bootstrap for General Stationary Observations. *Ann. Stat.* **17**, 1217–1241 (1989). Publisher: Institute of Mathematical Statistics.

146. Lahiri, S. N. Bootstrap Methods. In Lahiri, S. N. (ed.) *Resampling Methods for Dependent Data*, Springer Series in Statistics, 17-43 (Springer, New York, NY, 2003). https://doi.org/10.1007/978-1-4757-3803-2_2.
147. Wilks, D. S. Resampling hypothesis tests for autocorrelated fields. *J. Clim.* **10**, 65–82 (1997). Publisher: American Meteorological Society Section: Journal of Climate.
148. Wilks, D. S. Chapter 5 - Frequentist Statistical Inference. In Wilks, D. S. (ed.) *Statistical Methods in the Atmospheric Sciences (Fourth Edition)*, 143-207 (Elsevier, 2019). http://www.sciencedirect.com/science/article/pii/B9780128158234000055.
149. Benjamini, Y. & Hochberg, Y. Controlling the false discovery rate: a practical and powerful approach to multiple testing. *J. R. Stat. Soc.: Ser. B (Methodol.)* **57**, 289–300 (1995). Publisher: John Wiley & Sons, Ltd.
150. Sen, P. K. Estimates of the Regression Coefficient Based on Kendall's Tau. *J. Am. Stat. Assoc.* **63**, 1379–1389 (1968).
151. Rayner, N. A. et al. Global analyses of sea surface temperature, sea ice, and night marine air temperature since the late nineteenth century. *J. Geophys. Res. Atmos.* 108 (2003). https://doi.org/10.1029/2002JD002670.
152. Trenberth, K. E. The definition of El Niño in: Bulletin of the American Meteorological Society Volume 78 Issue 12 (1997). *Bull. Am. Meteorological Soc.* **78**, 2771–2778 (1997).
153. Saji, N. H., Goswami, B. N., Vinayachandran, P. N. & Yamagata, T. A dipole mode in the tropical Indian Ocean. *Nature* **401**, 360–363 (1999).

ACKNOWLEDGEMENTS

This work was supported by the Australian Climate Service. The authors acknowledge the Pangeo community for the open-source tools used in the analyses here.

AUTHOR CONTRIBUTIONS

D.R. devised the analysis, wrote the code, produced the figures and wrote the manuscript. D.R., A.B., D.I., R.M., D.M., J.R., D.S. and C.T. contributed to discussion of results and reviewing of the manuscript.

COMPETING INTERESTS

The authors declare no competing interests.

ADDITIONAL INFORMATION

Supplementary information The online version contains supplementary material available at https://doi.org/10.1038/s41612-022-00248-4.

Correspondence and requests for materials should be addressed to Doug Richardson.

Reprints and permission information is available at http://www.nature.com/reprints

Publisher's note Springer Nature remains neutral with regard to jurisdictional claims in published maps and institutional affiliations.